PCCP

PAPER

Inquiry of the electron density transfers in chemical reactions: a complete reaction path for the denitrogenation process of 2,3-diazabicyclo-[2.2.1]hept-2-ene derivatives†

Cite this: DOI: 10.1039/c5cp05518k

Vicent S. Safont, Patricio González-Navarrete,‡ Mónica Oliva and Juan Andrés

Received 15th September 2015,
Accepted 5th November 2015

DOI: 10.1039/c5cp05518k

www.rsc.org/pccp

A detailed study on all stages associated with the reaction mechanisms for the denitrogenation of 2,3-diazabicyclo[2.2.1]hept-2-ene derivatives (DBX, with X substituents at the methano-bridge carbon atom, X = H and OH) is presented. In particular, we have characterized the processes leading to cycloalkene derivatives through migration-type mechanisms as well as the processes leading to cyclopentil-1,3-diradical species along concerted or stepwise pathways. The reaction mechanisms have been further analysed within the bonding evolution theory framework at B3LYP and M05-2X/6-311+G(2d,p) levels of theory. Analysis of the results allows us to obtain the intimate electronic mechanism for the studied processes, providing a new topological picture of processes underlying the correlation between the experimental measurements obtained by few-optical-cycle visible pulse radiation and the quantum topological analysis of the electron localization function (ELF) in terms of breaking/forming processes along this chemical rearrangement. The evolution of the population of the disynaptic basin V(N1,N2) can be related to the experimental observation associated with the N═N stretching mode evolution, relative to the N_2 release, along the reaction process. This result allows us to determine why the N_2 release is easier for the DBH case *via* a concerted mechanism compared to the stepwise mechanism found in the DBOH system. This holds the key to unprecedented insight into the mapping of the electrons making/breaking the bonds while the bonds change.

1. Introduction

One of the key challenges in chemistry has been to characterize and then to understand the breaking and formation of chemical bonds along the course of a given chemical reaction. For such a purpose, a reaction mechanism describes in detail what is exactly happening at each stage (elementary reaction) of an overall chemical process (transformation) and, even more specifically, which bonds break (in the reactant) and form (in the product) along the reaction coordinate. Hence, the knowledge of the atom–atom mapping certainly constitutes the foundation for its establishing. In addition, chemical kinetics measurements have played a crucial role in determining unknown chemical processes, providing rate laws and rate constants that can then be used to derive a plausible reaction mechanism. Nevertheless, in some cases the elementary steps of a given reaction mechanism cannot be identified unambiguously since they are not experimentally accessible requiring the complement of a theoretical description for such complex chemical rearrangements.

Certainly, visualizing the progress of chemical reactions on their natural time scale can be considered the holy grail of chemical physics giving rise to the whole description of the reaction mechanism. Experimentally, the reaction path is difficult to map because it proceeds so quickly and therefore suitable spectroscopies are very demanding. In particular, some efforts have now been done by means of ultrafast electron diffraction or X-ray diffraction,[1] while advances in the area of attosecond physics[2] and real-time vibrational spectroscopy[3–5] by a few femtosecond pulse laser have been recently achieved. By means of this technique, the ultrashort visible pulse excites vibrational modes coherently in the electronic ground state through the stimulated Raman processes which precedes the reaction in the electronic ground state like the thermal excitation under heating. In particular, the mechanism of denitrogenation for 2,3-diazabicyclo[2.2.1]hept-2-ene (DBH) derivatives has been investigated using a visible 5 fs pulse laser.[3] There has

Departamento de Química Física y Analítica, Universitat Jaume I, Avda. Sos Baynat s/n, 12071, Castelló de la Plana, Spain

† Electronic supplementary information (ESI) available: Tables S1 and S2 with relative energy values for the stationary points found at four theoretical levels; Fig. S1–S4 with the ELF localization domain snapshots for points representing all SSDs found; DBH and DBOH cartesian coordinates; and the ELF mathematical model. See DOI: 10.1039/c5cp05518k

‡ Present address: Institut für Chemie, Technische Universität Berlin Straße des 17 Juni 135, 10623 Berlin, Germany. E-mail: andres@qfa.uji.es

been a long debate concerning a reasonable mechanism that describes this reaction because product formation could be achieved through a concerted or a stepwise mechanism. Thus, the process has been widely studied,[6–21] establishing that the corresponding reaction mechanism for thermal denitrogenation depends on the nature of substituents at the methano-bridge carbon atom of the DBH structure.[3,18,21,22] For electron donating substituents (X = –H and $–SiR_3$) the denitrogenation process takes place *via* concerted mechanisms, whereas σ electron withdrawing substituents (X = –F and $–OCH_2CH_3$) give rise to stepwise ones *via* diazenyl diradical intermediates.[3,18,21] The substituent effects have been explained based on computational studies in which the lowest electronic configuration of the singlet state of the resulting diradicals[18] has been invoked.

Motivated by these studies, our intention with the present work has been to study in greater detail the reaction mechanism for the thermal denitrogenation processes of DBH and DBOH under the domain of quantum chemical topology (QCT),[23] a subarea of quantum mechanics, based on the analysis of the gradient of scalar functions, following the seminal work of Bader.[24,25] This represents an alternative to understand and describe chemical reactivity based on well-defined physical entities accessible from experiments, in the case of charge distribution. In the framework of QCT, bonding evolution theory (BET) proposed by Krokidis *et al.*,[26] which combines the electronic localization function (ELF)[27,28] and Thom's catastrophe theory (CT),[26,29] has been employed to unravel the reaction mechanism and substituent effects.[30–42] To obtain a trustworthy picture, one must first perform computational studies, and then post-process the complicated information encoded in the accurate wave function in a way that facilitates chemical interpretation where concepts from QCT are used to provide insight into the molecular electronic structure and the changes in the electronic structure that accompany chemical processes.

It is worth noting that an important feature of BET is the ability to observe the flow of the electron density as the reaction proceeds; in other words, BET allows the monitoring of a chemical rearrangement along the reaction coordinate. One example of that corresponds to the thermal degenerate Cope rearrangement of semibullvalene,[43] where BET is capable of adequately predicting the order, direction, and asynchronicity of electron fluxes, providing rather valuable information of reaction mechanisms at the elementary level. Thus, within the broad scope of both experimental and theoretical investigations, the interest has been focused on extracting information about the evolution of the structure and energy along the reaction which may be insufficient to establish its electronic mechanism in detail. Indeed, certain vibrational modes can be directly associated with the presence of covalent bonds while their evolutions in the course of the reaction coordinate may be correlated with the information obtained from the BET analysis, and hence, an analysis could be desirable in such cases where reactions are too complex or too fast to be measured under *in situ* conditions due to slow and/or insensitive experimental techniques.

This work aims to contribute to the discussion on the nature of the reaction mechanism for the denitrogenation process in DBH and DBOH systems, assessing the usefulness of the BET protocol by comparing with previous results obtained by means of selective laser pulse experiments. Therefore, our focus is here to gain deeper insight into how electron density rearranges and how this rearrangement can be associated with chemical events such as the breaking/forming of chemical bonds, along the reaction progress. Thus, questions such as: (i) how could the electronic reorganization proceed along the reaction path, (ii) how this reorganization can be related to experimental data obtained by real-time vibrational spectroscopy?, (iii) how substituent effects (electron donating/withdrawing) are related to the electronic density flows, (iv) where and how do bond formation/breaking processes take place?, and (v) how the electronic reorganizations can be related to stepwise C–N bond cleavage *versus* concerted cleavage of the two C–N bonds?, may be answered and, admittedly, such a task is ambitious, but our hope is to provide a useful entry point to the growing literature by presenting a digestible account of key results to-date.

This paper is organized as follows: Section 2 describes the computational procedure, and Section 3 contains the results and discussions concerning the structure, energetics and ELF-topological properties of the different DBH and DBHO denitrogenation processes. Finally, we summarize our main conclusions in Section 4.

2. Computational procedure

Quantum chemical calculations have been performed using the Gaussian 09 suite.[44] We have selected the B3LYP[45–47] exchange–correlation functional for the geometry optimization of DBH, whereas for the DBOH system the M05-2X functional[48] was used. The 6-311+G(2d,p) basis set was employed for all atoms, while vibrational frequencies were calculated to characterize the structures as minimum or transition states (TSs) as well as to obtain the zero-point-point energy corrections. The capability of the B3LYP/6-311+G(2d,p) level to properly describe the decomposition process of DBH has been demonstrated because it predicts the same activation barrier (after the spin projection, see below) than the one calculated at the (6,6)CASPT2/6-31G(d)//(6,6)CASSCF level as performed by Houk *et al.*[20] On the other hand, B3LYP was not chosen for the DBOH system because it does not reproduce the second C–N bond cleavage as the rate-determining step of the stepwise mechanism, while the use of the M05-2X functional agrees with the results reported by Abe *et al.* by using the UCCSD/6-31G(d) level.[19]

Starting from the TS, the intrinsic reaction coordinate (IRC)[49,50] pathway is traced to their corresponding associated reactants and products. A mass-weighted step of 0.05 $amu^{1/2}$ bohr has been employed until the minimum was reached. For each point along the IRC, the wave function has been obtained and the ELF analysis has been performed by means of the TopMod package[51] considering a cubical grid of stepsize smaller than 0.05 bohr. The ELF basins are visualized using the Chimera program.[52] Due to the presence of diradical species along the IRC path, the stability of the wave function was checked

according to the procedure described by Bauernschmitt and Ahlrichs.[53] For the open-shell TS and/or intermediate obtained at the UDFT level, the broken symmetry[54,55] approach has been used as an approximation for multireference treatment. In addition a triplet calculation is performed to obtain E_t, while the projected low spin energy E_{ls} is calculated using the formula:

$$E_{ls} = E_t + \frac{2[E_{bs} - E_t]}{[2 - \langle S^2 \rangle_{bs}]} \quad (1)$$

E_{bs} corresponds to the energy of the broken-symmetry calculation, while $\langle S^2 \rangle_{bs}$ value corresponds to the total spin operator for the broken-symmetry solution, ranging from 0 when the valence electrons are paired to 1 in the ideal case of noninteracting spin in equivalent orbitals.

Previous theoretical studies have demonstrated that the ELF topological analysis is a valuable tool to gain fundamental insights from the breaking/forming processes along the reaction pathway.[30–41,43,56,57] The topological partition of the ELF gradient field[28] provides a basin of attractors, which are classified as core and valence basins. Core basins C(A) can be thought as atomic cores, while valence basins V(A) can be interpreted as bond and lone pairs, where A is the atomic symbol of the element. V(A), V(A,B) or V(A,B,C) are characterized by their coordination number with core basins (synaptic order) as monosynaptic, disynaptic or trisynaptic basins, respectively.[58] Thus, this description recovers the Lewis bonding model suggesting a graphical representation of the molecular system. A quantitative analysis is further achieved by integrating the electron density and the pair functions over the volume of the basin yielding basin populations (for details of the mathematical model of the ELF, see ESI†).

Along a reaction pathway (which links the chemical structures and therefore the topologies of the ELF gradient fields of the reactants with those of the products) the system experiences a series of structural stability domains (SSDs) within which all the critical points are hyperbolic separated by catastrophic points at which at least one critical point is non-hyperbolic. The bifurcation catastrophes occurring at these turning points are identified according to Thom's classification[29] which gives access to their unfolding, a compact polynomial expression which contains all the information about how the ELF may change as the control parameters change. In this way, a chemical reaction is viewed as a sequence of elementary chemical processes characterized by a catastrophe. These chemical processes are classified according to the variation of the number of basins μ and/or of the synaptic order σ of at least one basin. Details of the Thom's classification in chemical reactions have been described in detail elsewhere.[59]

3. Results and discussion

As stated before, the deazetization of DBH has been described as a concerted reaction mechanism giving rise to the cyclopentane 1,3-diyl species (DBH-diyl) *via* an open-shell singlet transition state (TSc-DBH), see Scheme 1. The open-shell singlet TSc-DBH is localized with an energy barrier of 37.1 kcal mol^{-1} and a $\langle S^2 \rangle$ value of 0.47. After the spin correction the energy barrier is predicted to be 32.3 kcal mol^{-1}, and in good agreement with previous energy barrier values reported, as aforementioned.[3,18,20] This reaction pathway has been predicted to be endothermic when the system reaches the DBH-diyl diradical. At the same time, DBH-diyl has been proposed to be the intermediate species for the formation of the closed-shell bicycle[2.1.0]pentane (BCP-DBH). The further steps from DBH-diyl to BCP-DBH fall outside the scope of the present work, and therefore we have not looked for the corresponding TS (or TSs). However, for the sake of completeness, the calculated values of energy for BCP-DBH are summarized in Table 1 and its geometries depicted in Fig. 1. As expected, BCP-DBH lays more than 30 kcal mol^{-1} under DBH-diyl species, and therefore the whole process from DBH to BCP-DBH is predicted to be exothermic.

In what refers to DBOH, B3LYP/6-31G(d) and CASSCF/6-31G(d) calculations[3,18,20] predict the thermal denitrogenation of DBOH as a stepwise reaction mechanism where the first C2–N1 bond cleavage results in a Morse-like potential, giving rise to a low-lying diazenyl diradical intermediate (DZ-DBOH), see Scheme 1. In contrast, at the UCCSD/6-31G(d) level, this TS associated with the first C2–N1 bond cleavage could be successfully optimized[19] (TSS1-DBOH), and even, it was calculated to be lower than that TS associated with the C4–N2 cleavage, indicating that the rate-determining step of the process corresponds to the second C–N bond breaking.[18,19] Thus, the reaction mechanism proceeds by means of two TSs associated with the first and second C–N bond cleavages (TSS1-DBOH and TSS2-DBOH, respectively). Interestingly, an increase of the size of the basis set at the M05-2X/6-311+G(2d,p) level allows the localization of the TS associated with the C2–N1 bond cleavage process, thus being consistent with UCCSD/6-31G(d) calculations. The respective energies of the localized species are summarized in Table 1, while its geometries are depicted in Fig. 2. The open-shell singlet TSS1-DBOH and TSS2-DBOH are localized with an energy barrier of 39.7 and 41.7 kcal mol^{-1}; nevertheless after the spin correction the energy barriers are predicted to be 34.1 and 40.3 kcal mol^{-1}, in good agreement with previous energy barrier values reported.[19] For comparison purposes, we also provide in the ESI† (Tables S1 and S2) the energetic values obtained by using the 6-31G(d) basis set for the reaction mechanisms studied for both systems, with both functionals.

On the other hand, the formation of cycloalquene products as a result of an X migration process coupled with the N_2 departure (for instance, for X = OEt) has also been reported.[19] Therefore, the migration reaction mechanisms have also been studied for DBH and DBOH. The migration reaction corresponds to a highly exothermic process and it entirely takes place *via* a closed-shell singlet state *via* TSm-DBX giving rise to cyclopentene derivatives (CP-DBX). These results can be associated with the strain on the original bicycle system that relaxes with the N_2 departure and the formation of the stable cyclopentene. Likewise, a relatively high activation barrier has been predicted (for details see Table 1), accounting for the TS complexity: in a single step three single bonds are broken and three bonds are formed: one of them of a single nature and the other two multiple. Therefore, both the fine tuning of

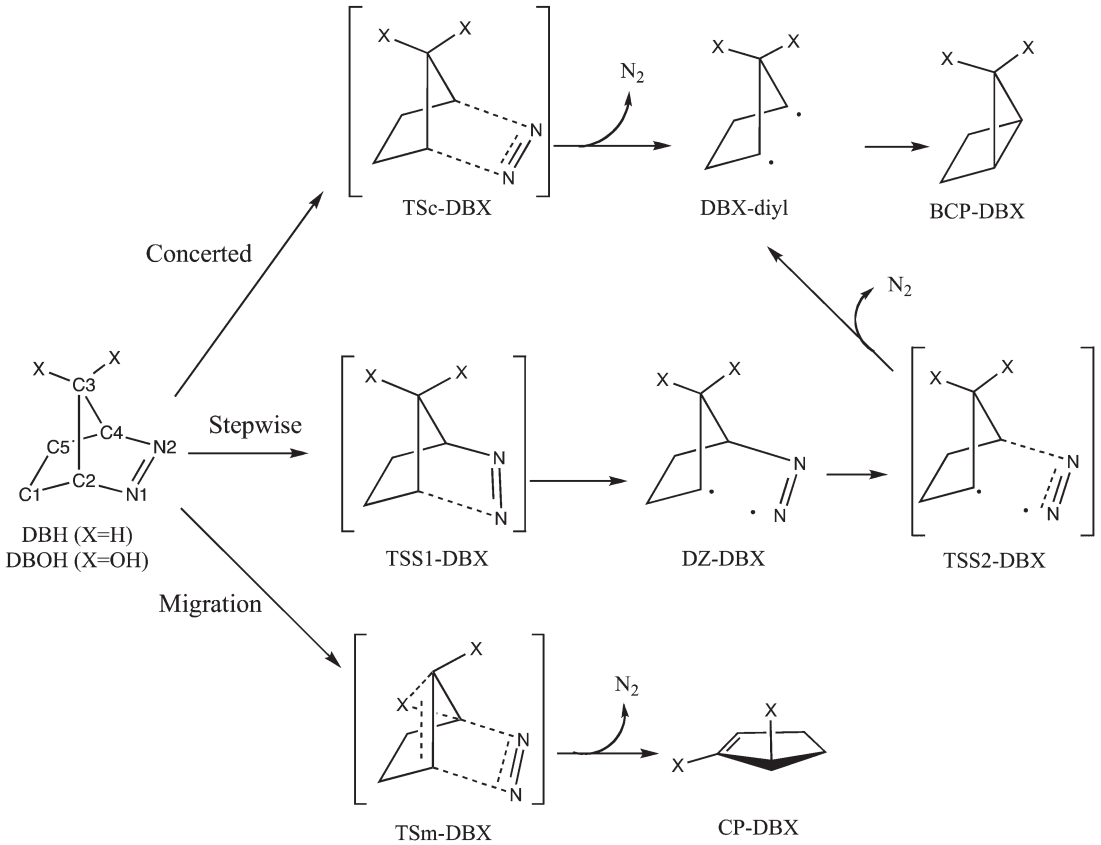

Scheme 1

Table 1 Relative (to DBH and DBOH in their closed-shell singlet state) energies (kcal mol^{-1}) of the stationary points found for the denitrogenation processes

Species	DBH[b]	Species	DBOH[c]
	Concerted reaction pathway		Stepwise reaction pathway
DBH	0.0	DBOH	0.0
TSc-DBH[a]	37.1	TSS1-DBOH[a]	39.7
DBH-diyl[a] + N_2	18.3	DZ-DBOH[a]	39.3
BCP-DBH + N_2	−12.2	TSS2-DBOHa	41.7
	Migration reaction pathway	DBOH-diyl[a] + N_2	22.5
TSm-DBH	42.9	BCP-DBOH	−8.3
CP-DBH + N_2	−43.5		Migration reaction pathway
		TSm-DBOH	71.8
		CP-DBOH + N_2	−37.6

[a] Open shell singlet species. [b] Calculated at the B3LYP/6-311+G(2d,p) level. [c] Calculated at the M05-2X/6-311+G(2d,p) level. Total energies of reactant species: DBH, −304 880 853 hartrees per particle; DBOH, −455 332 228 hartrees per particle.

the atom motions and a relatively high amount of energy are needed to reach TSm-DBX. Thus, the activation barriers for DBH and DBOH have been predicted to be 43.0 kcal mol^{-1} and 72.0 kcal mol^{-1}, respectively. This complexity explains the difficulty in locating this kind of TS either for the DBOH as well as for the X = OEt systems reported in the literature;[19] we have for the first time characterized these elusive stationary points thus giving a full theoretical description of the migration pathways.

ELF topological description

(a) Denitrogenation of DBH *via* the migration reaction pathway. The IRC energy profile associated with the migration pathway is depicted in Fig. 3 including six SSDs which are sketched in it from the perspective of the BET analysis: full lines and fat points represent disynaptic and monosynaptic basins, respectively, while hashed wedged bonds represent hydrogenated basins. The population of some basins along the IRC is shown in Fig. 4. Snapshots of the ELF localization domains for some selected points along the IRC, representative of the different SSDs, are reported in the ESI† (Fig. S1). In Fig. 5 a selection of them are offered.

At the DBH species (the left side of the energy profile in Fig. 3), 25 basins have been localized: 7 core basins, 8 hydrogenated basins, 8 disynaptic basins accounting for the C–C,

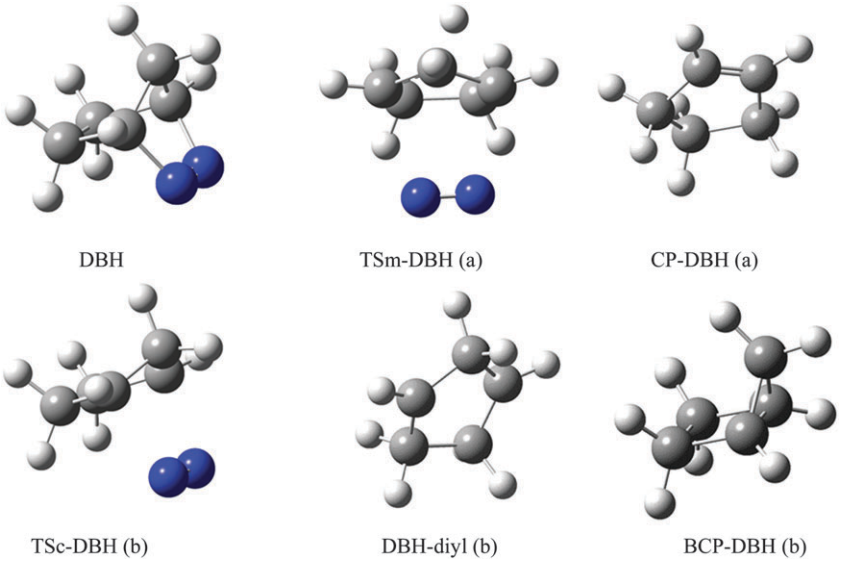

Fig. 1 Stationary points of the denitrogenation of DBH *via* (a) migration reaction pathway and (b) concerted reaction pathway. Color code; blue: nitrogen; grey: carbon; white: hydrogen.

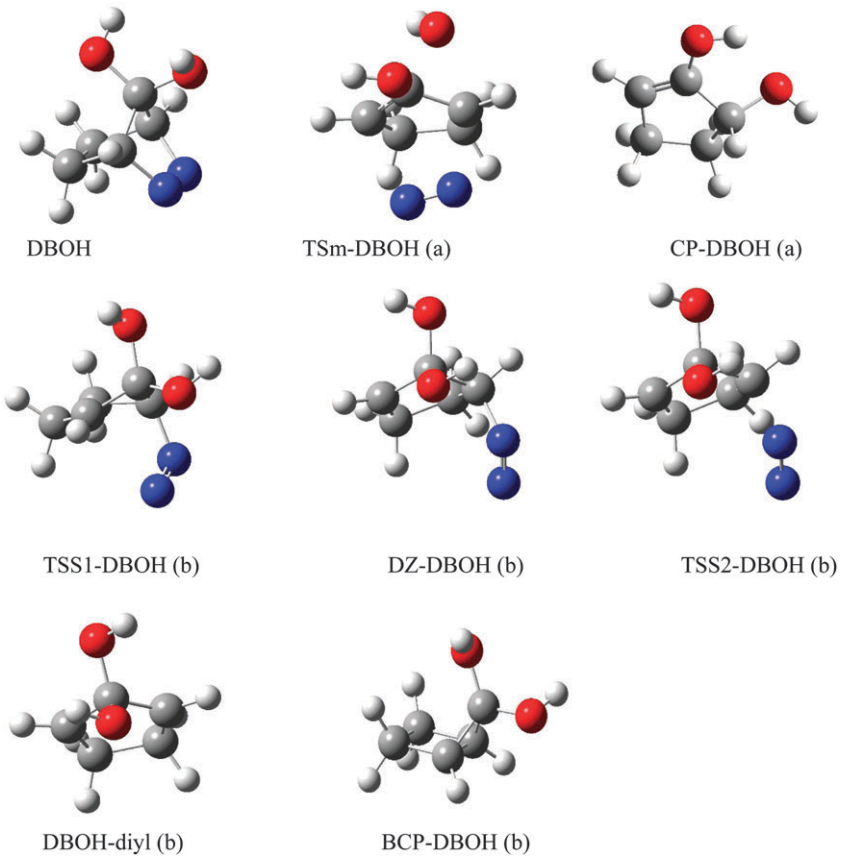

Fig. 2 Stationary points of the denitrogenation of DBOH *via* (a) migration and (b) stepwise pathways. Color code; blue: nitrogen; red: oxygen; gray: carbon; white: hydrogen.

C–N and N–N bonds, and 2 monosynaptic basins (V_1(N1) and V_1(N2)) accounting for the nitrogen lone pairs. The first ELF topological change (connecting SSD-I and SSD-II) comprises a simultaneous split of the disynaptic basins V(C2,N1) and V(C4,N2) by means of two simultaneous cusp-type catastrophes. As a consequence, the SSD-II begins with the creation of 4 new monosynaptic basins (V_2(N1), V_2(N2), V(C2), and V(C4)) whose total population equates the total one of the

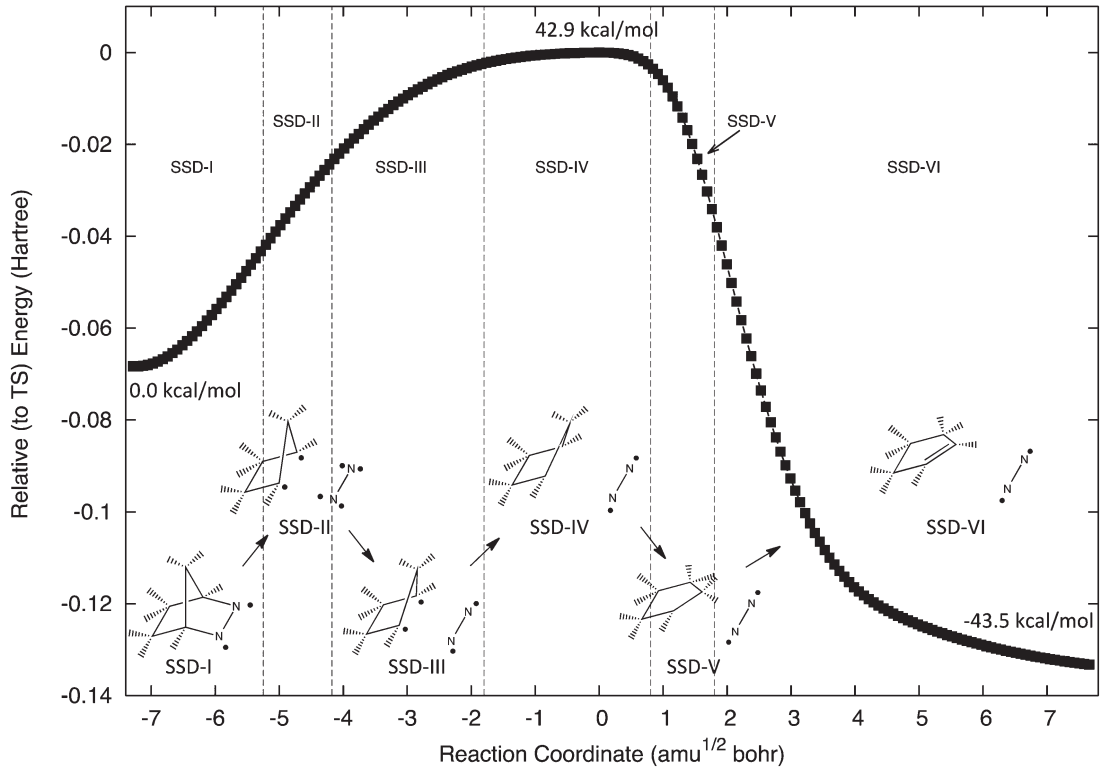

Fig. 3 Energy profile of the denitrogenation of DBH (left side) to give CP-DBH species and N_2 (right side), with marked SSDs, whose topology is sketched, obtained from the BET analysis.

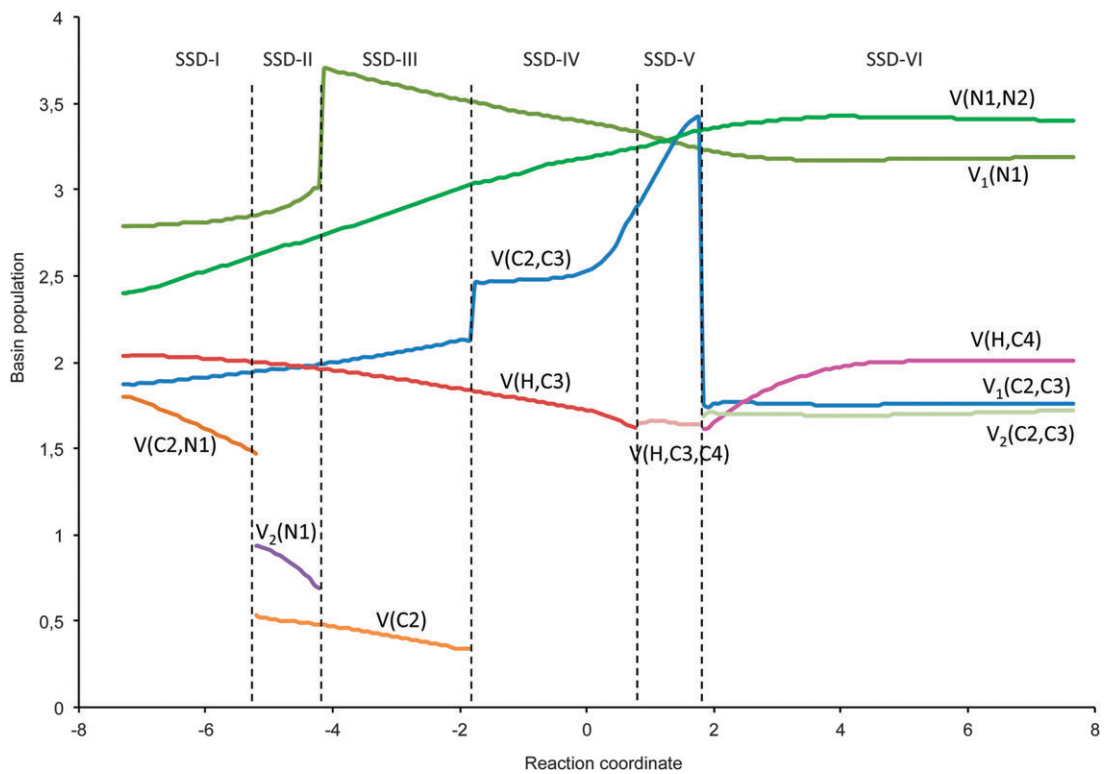

Fig. 4 Population of some basins along the IRC path of the denitrogenation of DBH *via* the migration reaction pathway as a function of reaction coordinate (amu$^{1/2}$ bohr)

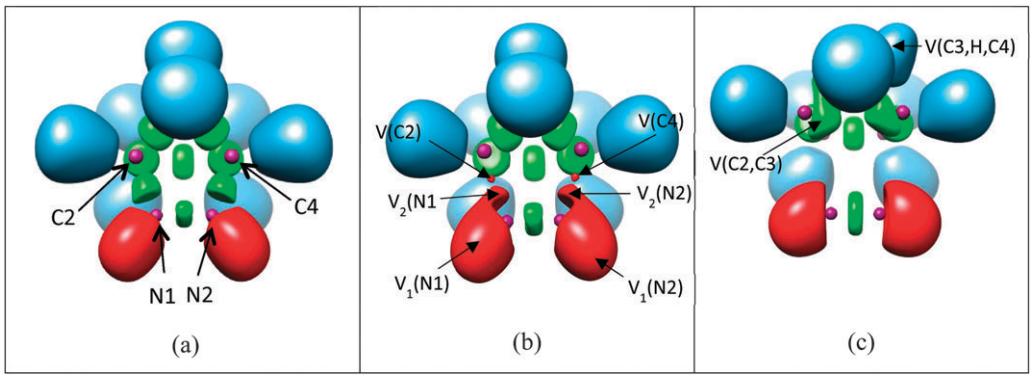

Fig. 5 Snapshots of the ELF localization domains (η = 0.8 isosurface except where indicated) for selected points along the IRC of the denitrogenation of DBH *via* the migration reaction pathway: (a) DBH belonging to SSD-I, (b) point at $s = -4.60$ amu$^{1/2}$ bohr (η = 0.785 isosurface) belonging to SSD-II, (c) point at s = 1.69 amu$^{1/2}$ bohr belonging to SSD-V. The color code is as follows: green, disynaptic basins; red, monosynaptic basins; blue, hydrogenated basins; and purple, core basins.

former disynaptic basins, surrounding their respective core basins (for comparison purposes see Fig. 5a and b). In Fig. 4 it can be sensed that the population of the disynaptic basin V(C2,N1) decreases in the course of SSD-I. The population of the V(C4,N2) is always the same compared to the population of the V(C2,N1) basin, so that it is not included. Along SSD-II the populations of that four monosynaptic basins diminish, being more acute than those of the monosynaptic basins V_2(N1) (and V_2(N2), not shown because it is always the same) with a concomitant increase in the population of the monosynaptic basin V_1(N1) (and V_1(N2), not shown for the same reason). Later, the second ELF topological change connecting SSD-II and SSD-III shows the annihilation of the monosynaptic basins V_2(N1) and V_2(N2) accounting for a double fold-type catastrophe, while the monosynaptic basins V_1(N1) and V_1(N2) acquire their respective populations which are reflected in a sudden increase of their populations when the system reaches SSD-III. The next ELF-topological event connecting SSD-III and SSD-IV corresponds to the simultaneous annihilation of the monosynaptic basins V(C2) and V(C4) accounting for a double fold-type catastrophe, while a sudden increase of the population of the disynaptic basin V(C2,C3) is sensed in Fig. 4. Then, in the course of SSD-IV the populations of the monosynaptic basins V_1(N1) and V_1(N2) decrease while the population of the disynaptic basin V(C2,C3) greatly increases: this disynaptic basin is anticipating its looming transformation. The population of the V(H,C3) basin continuously diminishes from the very beginning of the process, and when the system reaches SSD-V, it becomes trisynaptic V(C3,H,C4) thus indicating the hydride migration process from C3 towards C4 (see Fig. 5c). Finally, the last ELF-topological change discloses the transformation of the trisynaptic basin V(C3,H,C4) into the disynaptic basin V(H,C4), while the split of the disynaptic basin V(C2,C3) into two disynaptic basins $V_{1,2}$(C2,C3) (cusp-type catastrophe) is also observed. These changes can be clearly seen in Fig. 4.

Therefore, the description that emerges from the topological analysis of the DBH migration pathway reveals that the first chemical event that takes place is the simultaneous C–N bond breaking, and it is not until the reaction has advanced halfway that the hydride migration becomes apparent. The formation of the double bond between C2 and C3 atoms is the last chemical event along the whole process, whose driving force can undoubtedly be assigned to the N_2 release. On the other hand, the population of the disynaptic V(N1,N2) basin increases from 2.40*e* (at the DBH) up to 2.61*e* at the entrance of SSD-II. Its population continues to increase along SSD-II, SSD-III, SSD-IV (for instance, it has a value of 3.18*e* at TSm-DBH) and SSD-V, and it is not until halfway the SSD-VI that it acquires a stable value around 3.40*e*, very close to the value found for the N_2 molecule (3.36*e*).

(b) Denitrogenation of DBH *via* the concerted reaction pathway. The energy profile along the IRC for this pathway is depicted in Fig. 6 including 4 SSDs which are sketched from the perspective of ELF analysis. The evolution of the basin populations along the IRC is shown in Fig. 7, and snapshots of the ELF localization domains for some selected points along the IRC pathway, representative of some SSDs are presented in Fig. 8. In Fig. S2 (ESI†) snapshots of selected points representing all the SSDs found are reported.

Again, in this case the process begins with the simultaneous breaking of the two C–N bonds. The process undergoes the simultaneous split of the disynaptic basins V(C2,N1) and V(C4,N2) into four monosynaptic basins V(C2), V_2(N1), V(C4) and V_2(N2) by means of two cusp-type catastrophes. When the system reaches SSD-III, the simultaneous annihilation of the monosynaptic basins V_2(N1) and V_2(N2) (fold-type catastrophe) is observed, see Fig. 8a. The V(N1,N2) basin population increases from 2.40*e* up to 2.63*e* at the end of SSD-I, then up to 2.97*e* at the TSc-DBH, and finally it reaches a stable value at around 3.38*e*. Note that the topological evolution of the ELF field is practically identical to the migration reaction pathway until the system reaches the respective SSD-III; nevertheless is in the course of SSD-III where the biradicaloid nature of the system is sensed. To avoid overlap between monosynaptic basins V(C) and disynaptic basins V(C–H)[37,38,60,61] we have calculated the basin populations for α and β electrons separately. In the middle of the course of SSD-III, the populations of the monosynaptic basins V(C2) and V(C4) increase accounting

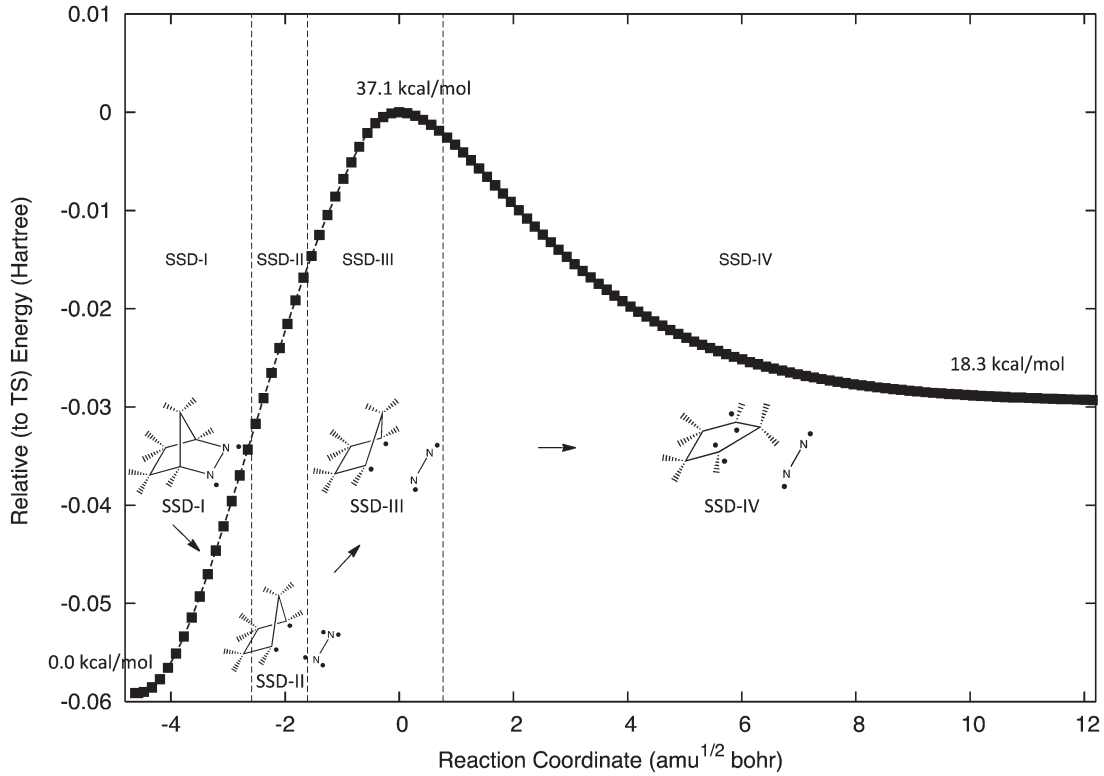

Fig. 6 Energy profile of the denitrogenation of DBH (left side), to give DBH-diyl species and N_2 (right side), with marked SSDs whose topology is sketched, obtained from the BET analysis.

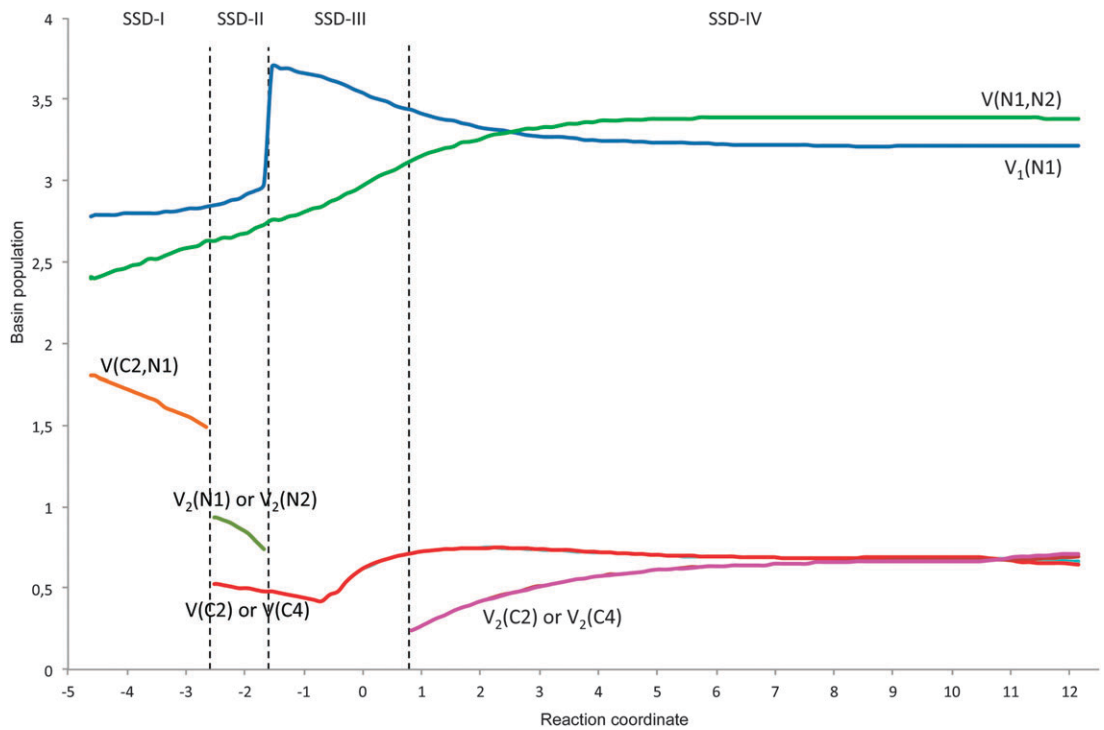

Fig. 7 Population of some basins along the IRC path of the denitrogenation of DBH *via* the concerted reaction pathway as a function of the reaction coordinate (amu$^{1/2}$ bohr).

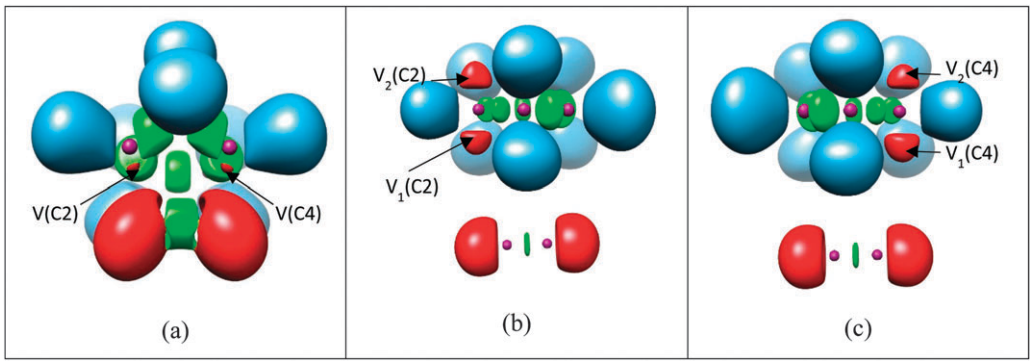

Fig. 8 Snapshots of some ELF localization domains for selected points along the IRC of the denitrogenation of DBH *via* the concerted reaction pathway (see DBH belonging to SSD-I in Fig. 5a): (a) TSc-DBH (η = 0.72 isosurface) belonging to SSD-III, (b) point at s = 12.15 amu$^{1/2}$ bohr (η = 0.86 isosurface, alpha electrons) belonging to SSD-IV, (c) point at s = 12.15 amu$^{1/2}$ bohr (η = 0.86 isosurface, beta electrons) belonging to SSD-IV.

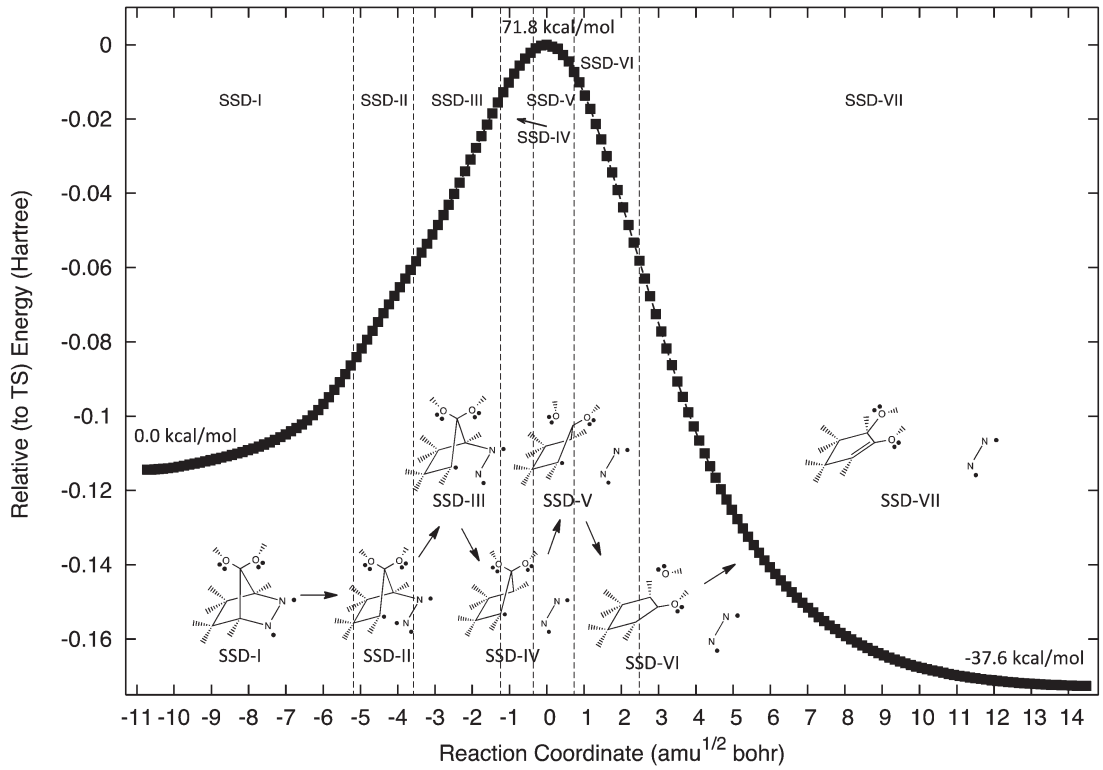

Fig. 9 Energy profile of the denitrogenation of DBOH (left side), to give CP-DBOH species and N_2 (right side), with marked SSDs whose topology is sketched, obtained from the BET analysis.

for a concentration of charge on C2 and C4 atoms. Finally, when the system reaches SSD-IV, two fold-type of catastrophes are observed due to the creation of two monosynaptic basins V_2(C2) and V_2(C4). These two new monosynaptic basins appear as a consequence of an excess of the charge density on C2 and C4 atoms indicating an electronic flux of the system towards these atoms (see Fig. 7 for a detailed evolution of the basin populations).

It is evident that both denitrogenation mechanisms begin with the C–N bond cleavage processes. But certainly, the denitrogenation *via* the migration pathway involves more chemical events (six SSDs), making this process energetically less favourable. Indeed, the charge density concentration between C2 and C3 atoms necessarily implies a hydride migration to reach the formation of CP-DBH and therefore this process needs a large energy to take place. In contrast, in the concerted mechanism the charge density flows directly towards C2 and C4 atoms upon C–N bond cleavages, avoiding thus any additional internal chemical rearrangement. As a consequence, the concerted reaction pathway allows better electron density redistribution in the course of the process which is reflected in a more favourable energy demand compared to the migration rearrangement.

(c) Denitrogenation of DBOH *via* the migration reaction pathway. The energy profile along the IRC reaction pathway is depicted in Fig. 9 including seven SSDs that are sketched

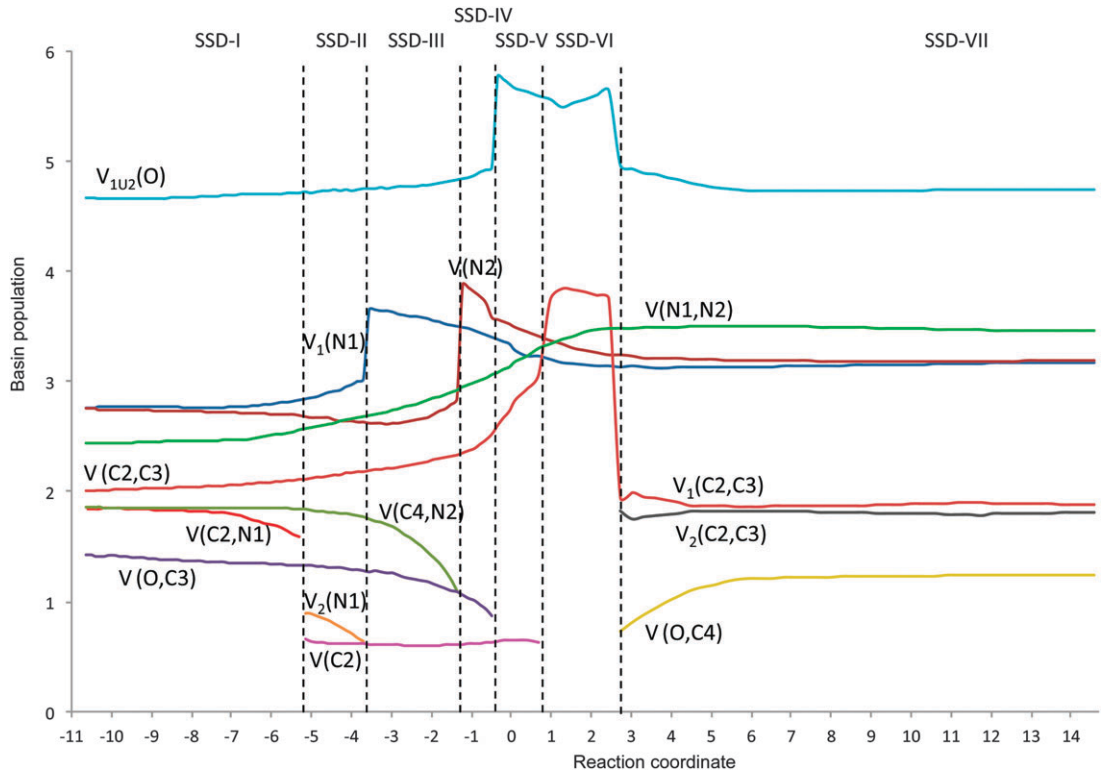

Fig. 10 Population of some basins along the IRC path of the denitrogenation of DBOH *via* the migration reaction pathway as a function of reaction coordinate (amu$^{1/2}$ bohr).

according to the perspective of the BET analysis. Evolution of the basin populations along the IRC pathway is shown in Fig. 10. Snapshots of some ELF-SSDs are presented in Fig. 11, and the whole set of pictures can be found in Fig. S3 (ESI†).

As observed in Fig. 9, the C–N bond cleavages do not occur simultaneously. Thus, the first ELF-topological change, connecting SSD-I and SSD-II, shows the split of the disynaptic basin V(C2,N1) into two monosynaptic basins V(C2) and V_2(N1) by means of a cusp-type catastrophe. Then, in the course of SSD-II the population of the monosynaptic basin V(C2) remains practically constant, whereas the population of the monosynaptic basin V_2(N1) diminishes. When the system reaches SSD-III a fold-type catastrophe is observed accounting for the annihilation of the monosynaptic basin V_2(N1) (see Fig. 11b); its population is now incorporated in the former monosynaptic basin V_1(N1) that experiences a sudden increase in its population, see Fig. 10. In the course of SSD-III the population of the disynaptic basin V(C2,C3) slightly increases, while the pronounced diminution of the population of the disynaptic basin V(C4,N2) finally ends up in the annihilation of this disynaptic basin when the system reaches SSD-IV, by means of a fold-type catastrophe (see also Fig. 11c); as a consequence a sudden increase of the monosynaptic basin V(N2) is also sensed. Next, when the system reaches SSD-V the ELF field undergoes a

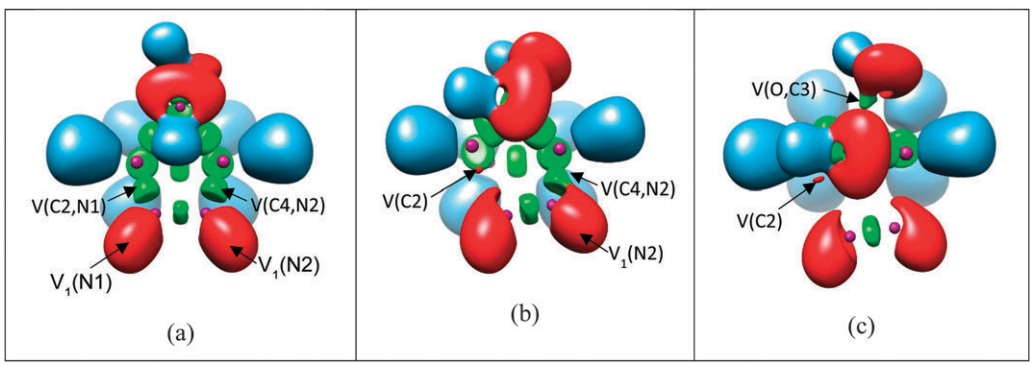

Fig. 11 Snapshots of some ELF localization domains for selected points along the IRC of the denitrogenation of DBOH *via* the migration pathway: (a) DBOH belonging to the SSD-I domain (η = 0.8 isosurface); (b) point at s = −2.48 amu$^{1/2}$ bohr belonging to SSD-III (η = 0.78 isosurface); (c) point at s = −0.88 amu$^{1/2}$ bohr belonging to SSD-IV (η = 0.79 isosurface).

topological change disclosing the annihilation of the disynaptic basin V(O,C3) (fold-type catastrophe) which accounts for the migration of the OH group from C3 towards C4; likewise an increase in the population of the monosynaptic basins $V_{1,2}(O)$, which belong to the mentioned OH group, is observed. In Fig. 10 the population of these two monosynaptic basins $V_{1,2}(O)$ are depicted as a whole ($V_{1U2}(O)$, see the pale blue line). Upon annihilation of the disynaptic basin V(O,C3), a diminution in the population of the basins V(N2), $V_{1,2}(O)$ and $V_1(N1)$ is observed, accompanied by a pronounced increase in the population of the disinaptic basin V(C2,C3). Subsequently, when the system reaches SSD-VI, a fold-type catastrophe due to the annihilation of the monosynaptic basin V(C2) is found, its respective population being transferred to the disynaptic basin V(C2,C3). After that, a slight diminution in the population of the disynaptic basin V(C2,C3) is sensed concomitantly with an increase in the sum of the population of the monosynaptic basins $V_{1,2}(O)$. When SSD-VII is reached, two simultaneous catastrophes occur: (i) the split of the disynaptic basin V(C2,C3) into two disynaptic basins $V_{1,2}(C2,C3)$ accounts for the dual character of the C2–C3 bond (cusp-type catastrophe) and (ii) the creation of the disynaptic basin V(O,C4) (fold-type catastrophe), which reflects the migration process of the OH group. This last ELF topological change is accompanied by a diminution of the populations of the two monosynaptic basins $V_{1,2}(O)$. In addition, the population of the disynaptic basin V(N1,N2) (see the light green line in Fig. 10) reveals a slight increment in the early SSDs, but a more pronounced increase upon annihilation of the disynaptic basin V(C4,N2). Thus, when the system reaches the TS the population of the disynaptic basin V(N1,N2) is predicted to be 3.18*e*, reaching a stable value of around 3.5*e* in the late SDDs. This value is roughly maintained along SSD-VII until the end of the IRC path, where a final population value of 3.46*e* is predicted.

A comparison can be done between DBH and DBOH migration processes. Certainly in the DBH case, the C–N bond cleavages take place simultaneously at the beginning of the process, giving rise directly to the hydride migration, and then to end up in the formation of CP-DBH. However, the thermal migration process of DBOH entails one more step (SSDs), making this thermal rearrangement more complex and energetically less favourable, see Table 1. Indeed, the C–N bond cleavages occur in different stages of the process. Upon the first C2–N1 bond cleavage, the system continues with some basin rearrangements until reaching the second C–N bond breaking. Therefore, the presence of the OH substituents certainly does not favour the migration rearrangement. Furthermore, the OH migration takes place along two SSDs, while the hydride migration is completed within a single SSD. In both cases, the migration process is not completed until the formation of the double bond between C2 and C3 is reached.

(d) Denitrogenation of DBOH *via* the stepwise reaction pathway. The energy profile for this pathway and its six SSDs are depicted in Fig. 12a and b. Fig. 12a corresponds to the energy profile from DBOH (left side) towards DZ-DBOH species (right side) *via* TSS1-DBOH. Fig. 12b corresponds to the energy profile from DZ-DBOH (left side) towards DBOH-diyl (right side) *via* TSS2-DBOH. It is worth mentioning that two structures for DZ-DBOH have been predicted for each energy profile. They do not exactly match, because they exhibit different rotation angles around the C4–N2 bond. However, their ELF topologies are the same, and hence belong to the same SSD, see below. In addition, the populations for the different basins are very similar in either conformation, as can be qualitatively sensed in Fig. 13a (right side) and b (left side). From a quantitative viewpoint, the maximum discrepancy (of only 0.1*e*) has been found for the V(N2) basin population. The SSDs found are sketched in Fig. 12 from the perspective of ELF analysis. The populations of some basins are shown in Fig. 13, while snapshots of the ELF localization domains for some selected points along the pathway from DBOH to DBOH-diyl, representative of the different SSDs, are presented in Fig. 14.

An analysis of the results points out that the first ELF topological change accounts for the C2–N1 bond cleavage. As a consequence, the population of the disynaptic basin V(N1,N2) only increases 0.12*e*. The split of the disynaptic basin V(C2,N1) into two monosynaptic basins $V_1(C2)$ and $V_2(N1)$ (cusp-type catastrophe) is observed when SSD-II is reached (see Fig. 13a). Upon C2–N1 bond cleavage the system undergoes an excess of charge density on C2 which is reflected in the creation of a new monosynaptic basin $V_2(C2)$ (fold-type catastrophe) when SSD-III is reached. Note that TSS1-DBOH, DZ-DBOH and TSS2-DBOH belong to the same SSD. Then, in the course of SSD-III a pronounced increase of the population of the monosynaptic basin V(N2) (Fig. 13b) is observed and, in contrast, a decrease in the population of the disynaptic basin V(C4,N2) is also sensed. The disynaptic basin V(N1,N2) increases its population up to 2.71*e* at TSS1-DBOH, 2.76*e* (avg.) at DZ-DBOH, and 3.00*e* at TSS2-DBOH. Subsequently, the annihilation of the disynaptic basin V(C4,N2) is sensed when SSD-IV is reached. Interestingly, the second C–N bond cleavage takes place immediately after the system overcomes the TSS2-DBOH. The SSD-IV is very short and principally reflects a pronounced change in the population of the monosynaptic basin $V_1(N1)$. As result, the annihilation of the monosynaptic basin $V_2(N1)$ occurs when the SSD-V is reached. Finally, the last ELF topological change arises as a consequence of an excess of charge density on C4 which is reflected in the creation of the monosynaptic basin $V_2(C4)$ (fold-type catastrophe) when SSD-VI is reached.

The DBH concerted pathway and the DBOH stepwise pathway can be compared since both denitrogenation processes result in DBH-diyl and the DBOH-diyl species. As described, the presence of two hydroxyl groups on C3 dramatically alters the denitrogenation process. In the DBH case the C–N bond cleavages occur simultaneously, confirmed with the present ELF topological study. Four SSDs have been characterized accounting for the chemical events that take place in the way from DBH to DBH-diyl. However, in the DBOH case one of the C–N bonds break first, initiating a cascade of chemical events that take place in the way from DBOH to DBOH-diyl, including a transition structure that makes possible the formation of the intermediate DZ-DBOH, the passage through a second transition structure accounting for the second C–N bond breaking,

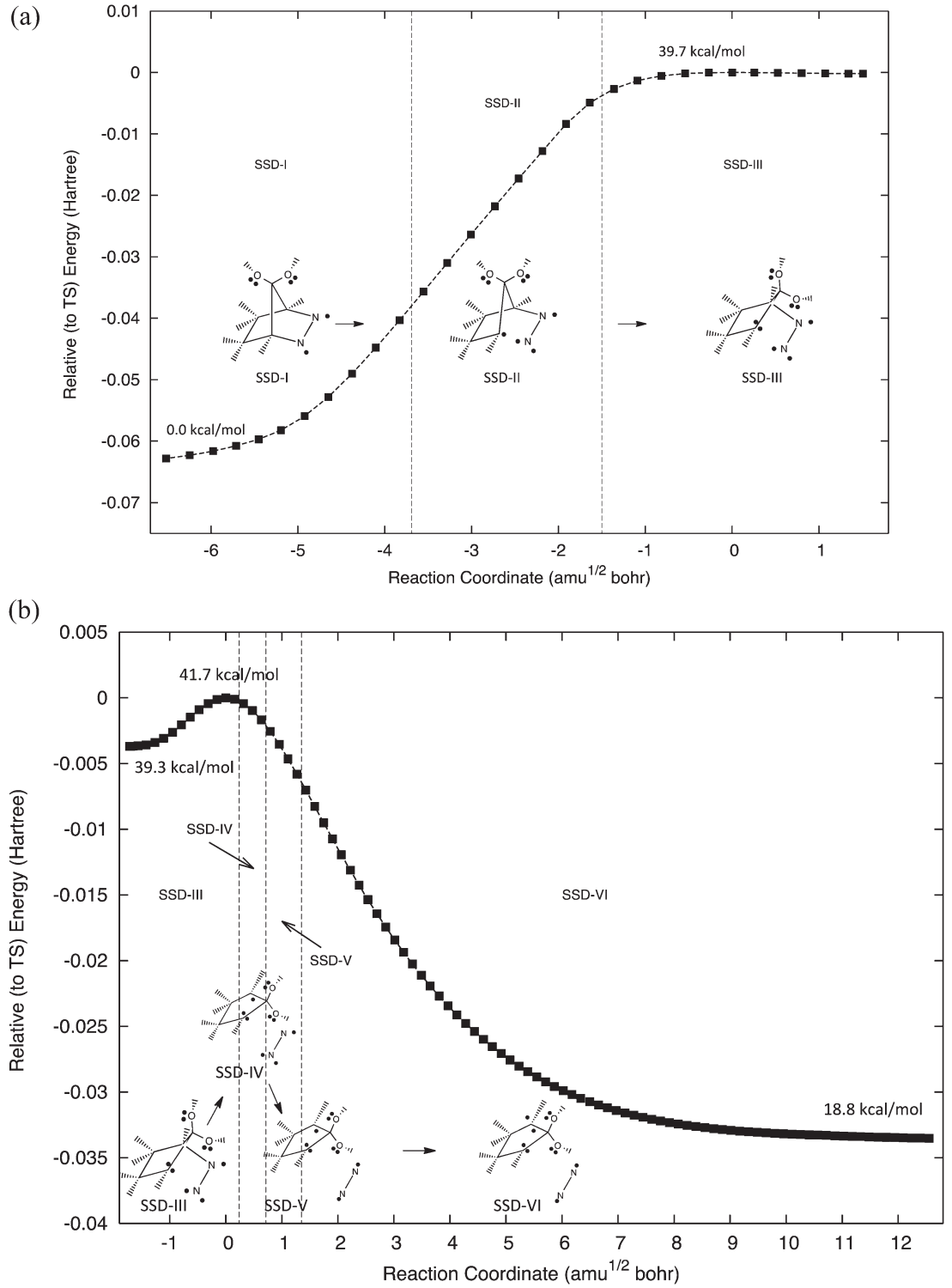

Fig. 12 (a) Energy profile for the denitrogenation of DBOH (left side) to give DZ-DBOH (right side), *via* TSS1-DBOH species, and (b) energy profile for the DZ-DBOH (left side) evolution to the DBOH-diyl species plus N_2 (right side), *via* TSS2-DBOH. Both energy profiles have been calculated by means of the IRC method. The SSD topology obtained from the BET analysis is sketched.

and the final electronic rearrangements to reach the final DBOH-diyl species.

Interestingly, the population of the disynaptic basin V(N1,N2) can provide a good correlation with experiments. Indeed, when the simultaneous C–N bond cleavages take place in DBH the population of the disynaptic basin V(N1,N2) is predicted to be 2.63*e*, whereas for the DBOH these are predicted to be 2.58*e* and 3.06*e* in the first and the second C–N bond

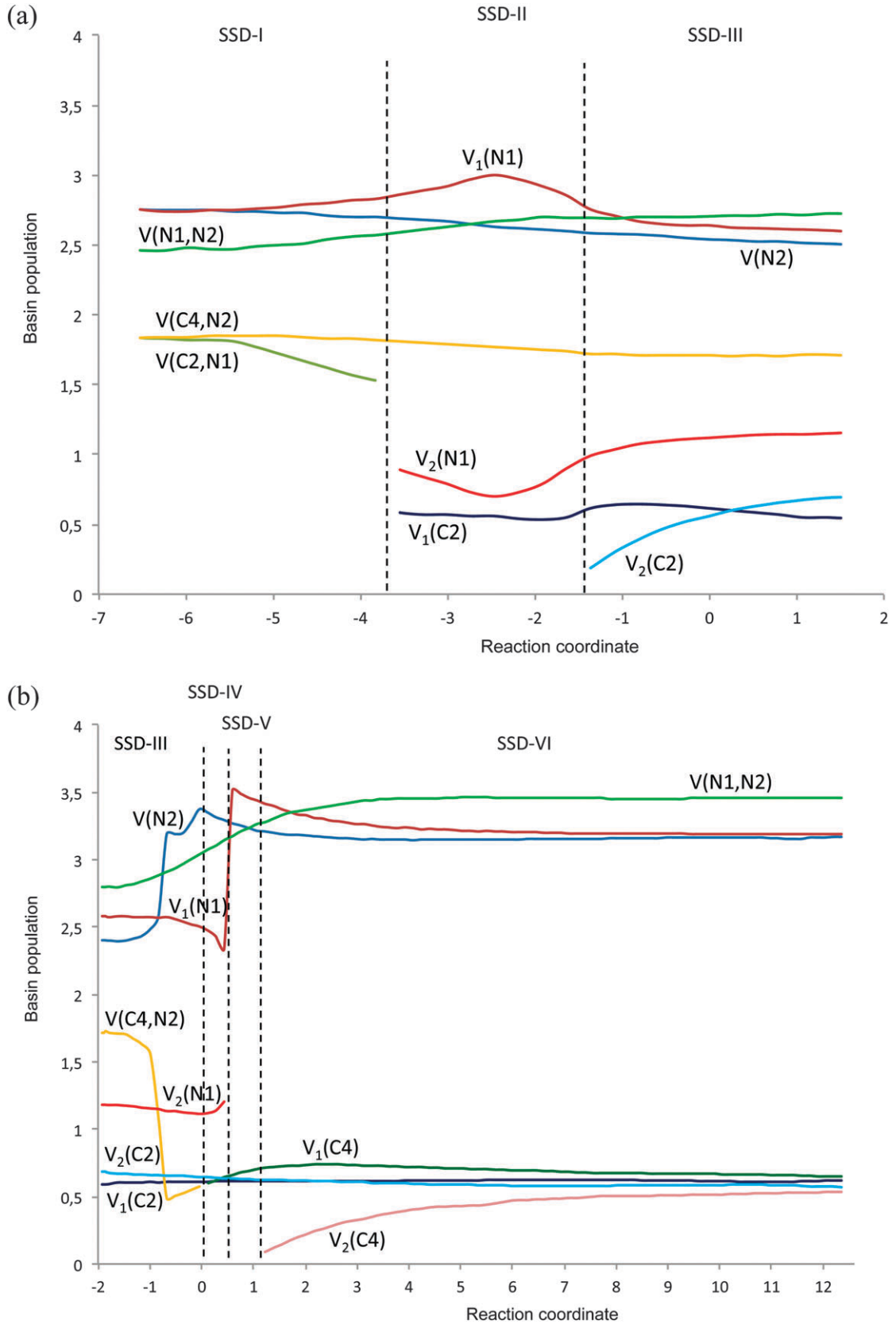

Fig. 13 (a) Population evolution of some basins along the IRC from DBOH to DZ-DBOH, and (b) population evolution of some basins along the IRC of the DBOH denitrogenation process *via* the stepwise reaction pathway, both as a function of reaction coordinate (amu$^{1/2}$ bohr).

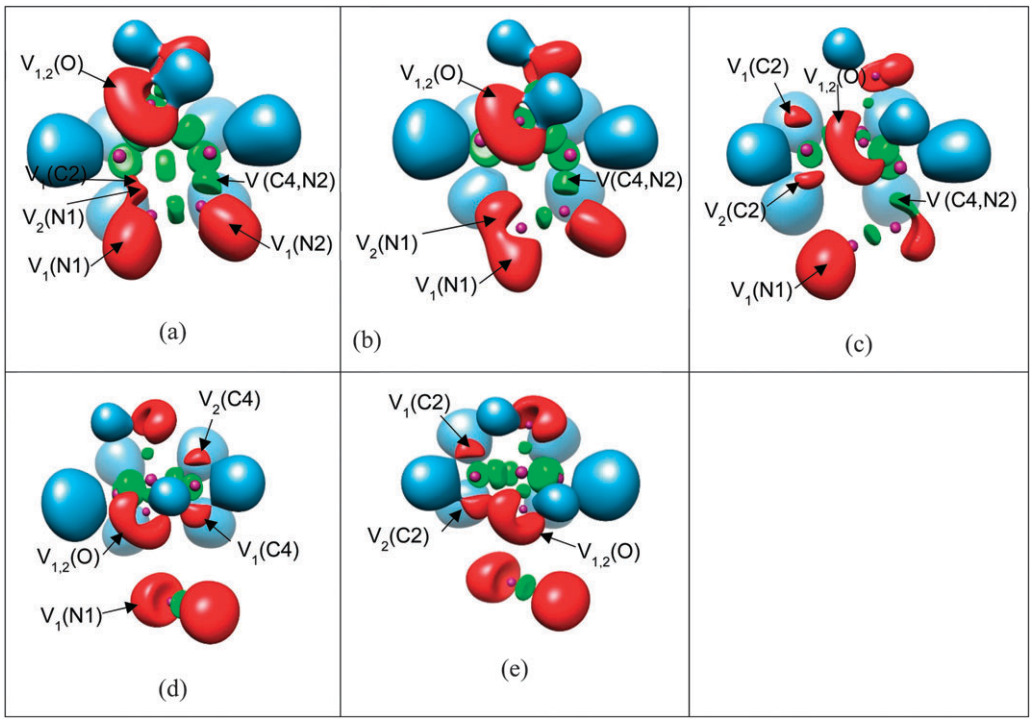

Fig. 14 Snapshots of the ELF localization domains (η = 0.8 isosurface except where indicated) for selected points along the IRC of the DBOH denitrogenation process *via* the stepwise reaction pathway (see DBOH belonging to SSD-I in Fig. 11a). (a) Point belonging to SSD-II; (b) TSS1 belonging to SSD-III (alpha electrons); (c) TSS1 belonging to SSD-III (η = 0.857 isosurface beta electrons). (d) DBOH-diyl species plus N_2, belonging to SSD-VI (η = 0.84 isosurface, alpha electrons); (e) DBOH-diyl species plus N_2, belonging to SSD-VI (η = 0.84 isosurface, beta electrons).

cleavage, respectively. The greater population of the disynaptic basin V(N1,N2) before the first C–N breaking found for the DBH correlates with the experimental observation of a greater wavenumber observed for the N═N stretching in the DBH (1950 cm^{-1}) compared to DBOH (1750 cm^{-1}). This also holds true in this basin population of the respective transition states and intermediates (at TSc-DBH = 2.97*e*; at TSS1-DBOH = 2.70*e*; at DZ-DBOH = 2.76*e*; and at TSS2-DBOH = 3.00*e*).

Finally, a last question remains to be answered: can the topological analysis shed some additional light in what refers to why the presence of the OH substituents push the denitrogenation process through a stepwise mechanism instead of through a concerted process? We have found neither a concerted process for the denitrogenation of the DBOH, nor a stepwise mechanism for the denitrogenation of DBH, and hence we cannot make a direct comparative analysis. However, the answer to that question should be intimately related to the answer of this alternative one: why the C–N bonds do break simultaneously in the DBH denitrogenation processes and consecutively in the DBOH case? The analysis of the population values of the disinaptic V(C2,N1) and V(C4,N2) basins along the reaction coordinate provides the desired clues: in both DBH denitrogenation processes, the population of the disynaptic basin V(C2,N1) is maintained always identical to the population of the V(C4,N2) basin, likewise the molecular symmetry that is maintained until these disynaptic basins disappear accounting for the C–N ruptures. Therefore, the N_2 departure takes place in a concerted manner without symmetry loss. It should be noted that in the migration mechanism the H motion takes place after the N_2 departure, as has been shown, and hence the inherent symmetry loss associated with this H displacement does not affect the C–N ruptures. However, in the DBOH denitrogenation processes, the population values of these disynaptic basins are slightly different for each other from the very beginning. And, as it is apparent from Fig. 10 and 13a, the basin with the initial lowest population of these two basins is the one that disappears first. The population difference must be due to the particular orientation of the monosynaptic V(O) basins belonging to the OH substituents on C3 (see Fig. 11a), that are not symmetrically placed and influence in a different manner the two molecule moieties, pushing and pulling the electron flow and making the two C–N bonds different. Hence, the reason for the asynchronous rupture of the two C–N bonds in the DBOH denitrogenation processes would lie on the asymmetry in the population of the V(C,N) basins, which in turn is caused by the particular orientation of the V(O) monosynaptic basins of the OH substituents on C3. In this way, one of the C–N bonds breaks first and therefore a different topological description of the denitrogenation processes of DBOH is obtained which involve more SSDs compared to DBH. We have included in the supporting material the cartesian coordinates of the optimized DBH and DBOH.

4. Conclusions

All stages of the denitrogenation processes of 2,3-diazabicyclo-[2.2.1]hept-2-ene derivatives have been studied by means of BET, based on topological analysis of the ELF and CT. This

procedure yields substantial information about chemical bonding along the reaction pathway, and allows us to investigate in detail the corresponding reaction pathways and to understand the flow of electrons that attends the process. From the experimental side, this chemical reaction has been analysed by a visible 5 fs pulse laser, allowing the characterization of the time-dependent frequency shifts of relevant molecular vibrational modes, that can be related to the progress of the V(N1,N2) basin population along the reaction pathway. Our results are capable of explaining why the DBH denitrogenation takes place *via* a simultaneous C–N bond breaking mechanism, and rationalize the observations made for the DBH concerted denitrogenation pathway compared to the stepwise DBOH denitrogenation process.

A concerted denitrogenation process was found in the thermolysis of the DBH; however, a stepwise nitrogen dissociation process was obtained for the denitrogenation process of the DBOH. Present theoretical results agree well with the experimental predictions, and the main conclusions of the present work can be summarized as follows: (i) we have for the first time (to our knowledge) characterized the TSs for the denitrogenation of DBH derivatives through migration-type pathways. (ii) We have noticed that the use of the extended basis set is necessary for the characterization of some stationary points along the reaction processes. (iii) The description that emerges from BET analysis of the DBH migration pathway reveals that the first chemical event is the simultaneous two C–N bond breaking process. After that, the next chemical event corresponds to the hydride migration process that becomes apparent when the reaction has advanced halfway. The double C3–C4 bond development is the last chemical event along the whole process. (iv) For the DBH concerted pathway the same behaviour can be observed: the process begins with the simultaneous C–N bond breaking process, and the rest of the events take place well afterwards and mainly affect the monosynaptic basins. (v) The presence of the OH substituents greatly changes the intimate electronic mechanism for the migration pathway and the C–N bond breaking processes takes place in two different stages of the process. The series of chemical events begin with the breaking of one C–N bond, continues with some basin rearrangements before the second C–N bond breaks, thereafter the OH leaves and its migration is not completed until the double bond formation has taken place, (vi) on the other hand, for the DBOH stepwise denitrogenation process, it can be sensed that TSS1-DBOH is very late with respect to the first C–N bond breaking process, and from the ELF electronic point of view, TSS1-DBOH shares the same topological domain with DZ-DBOH and TSS2-DBOH. Interestingly, the breaking process of C4–N2 occurs immediately after the system overcomes the TSS2-DBOH. Also in this case, as it happened with the migration pathway, the presence of the two hydroxyl groups on C3 completely changes the reaction mechanism for the denitrogenation processes leading to the diradical intermediate: in the DBH case the two C–N bonds break simultaneously, and four SSDs have been characterized accounting for the chemical events that take place in the way from DBH to DBH-diyl. However, in the DBOH case one of the C–N bonds breaks first, initiating a cascade of chemical events that take place in the way from DBOH to DBOH-diyl, including a transition structure that makes possible the formation of the intermediate DZ-DBOH, its configuration change, the passage through a second transition structure accounting for the second C–N bond breaking, and the final electronic rearrangements to reach the final DBOH-diyl species, (vii) the evolution of the population of the V(N1,N2) disynaptic basin can be related to the experimental data relative to the N_2 release, and our results nicely correlate with the experimental findings explaining why the N_2 release is easier for DBH *via* a concerted mechanism compared to the stepwise mechanism found in DBOH. (viii) Our results suggest that the reason for the different denitrogenation mechanisms (concerted *versus* stepwise) taking place in these systems would lie on the asymmetry in the initial population of the V(C,N) basins, which in turn is caused by the particular orientation of the V(O) monosynaptic basins of the OH substituents on C3.

The calculations have thus provided a deep insight into the nature of the denitrogenation processes. This is a nice guide study to elucidate the mechanism of chemical reactions, and it is a critical step in the analysis of reaction pathways and rates.

Acknowledgements

The authors are grateful to Generalitat Valenciana for PrometeoII/2014/022 and ACOMP/2015/102 projects, Ministerio de Economía y Competitividad (Spain) for project CTQ-2012-36253-C03-02, and Universitat Jaume I for project P1·1B2013-40. The authors are also grateful to the Servei d'Informàtica, Universitat Jaume I for generous allocation of computer time. P.G.-N. acknowledges support from the Alexander von Humboldt Foundation.

References

1 H. N. Chapman, P. Fromme, A. Barty, T. A. White, R. A. Kirian, A. Aquila, M. S. Hunter, J. Schulz, D. P. DePonte, U. Weierstall, R. B. Doak, F. R. N. C. Maia, A. V. Martin, I. Schlichting, L. Lomb, N. Coppola, R. L. Shoeman, S. W. Epp, R. Hartmann, D. Rolles, A. Rudenko, L. Foucar, N. Kimmel, G. Weidenspointner, P. Holl, M. Liang, M. Barthelmess, C. Caleman, S. Boutet, M. J. Bogan, J. Krzywinski, C. Bostedt, S. Bajt, L. Gumprecht, B. Rudek, B. Erk, C. Schmidt, A. Hömke, C. Reich, D. Pietschner, L. Strüder, G. Hauser, H. Gorke, J. Ullrich, S. Herrmann, G. Schaller, F. Schopper, H. Soltau, K.-U. Kühnel, M. Messerschmidt, J. D. Bozek, S. P. Hau-Riege, M. Frank, C. Y. Hampton, R. G. Sierra, D. Starodub, G. J. Williams, J. Hajdu, N. Timneanu, M. M. Seibert, J. Andreasson, A. Rocker, O. Jönsson, M. Svenda, S. Stern, K. Nass, R. Andritschke, C.-D. Schröter, F. Krasniqi, M. Bott, K. E. Schmidt, X. Wang, I. Grotjohann, J. M. Holton, T. R. M. Barends, R. Neutze, S. Marchesini, R. Fromme,

S. Schorb, D. Rupp, M. Adolph, T. Gorkhover, I. Andersson, H. Hirsemann, G. Potdevin, H. Graafsma, B. Nilsson and J. C. H. Spence, *Nature*, 2010, **470**, 73–77.

2 F. Krausz and M. Ivanov, *Rev. Mod. Phys.*, 2009, **81**, 163–234.

3 M. Abe, I. Iwakura, A. Yabushita, S. Yagi, J. Liu, K. Okamura and T. Kobayashi, *Chem. Phys. Lett.*, 2012, **527**, 79–83.

4 I. Iwakura, *Phys. Chem. Chem. Phys.*, 2011, **13**, 5546–5555.

5 I. Iwakura, A. Yabushita and T. Kobayashi, *Chem. Lett.*, 2010, **39**, 374–375.

6 P. S. Engel, *Chem. Rev.*, 1980, **80**, 99–150.

7 W. R. Roth and M. Martin, *Liebigs Ann. Chem.*, 1967, **702**, 1.

8 W. R. Roth and M. Martin, *Tetrahedron Lett.*, 1967, 4695–4698.

9 E. L. Allred and R. L. Smith, *J. Am. Chem. Soc.*, 1969, **91**, 6766–6775.

10 W. Adam, T. Oppenlander and G. Zang, *J. Org. Chem.*, 1985, **50**, 3303–3312.

11 B. A. Lyons, J. Pfeifer, T. H. Peterson and B. K. Carpenter, *J. Am. Chem. Soc.*, 1993, **115**, 2427–2437.

12 M. B. Reyes and B. K. Carpenter, *J. Am. Chem. Soc.*, 1998, **120**, 1641–1642.

13 N. Yamamoto, M. Olivucci, P. Celani, F. Bernardi and M. A. Robb, *J. Am. Chem. Soc.*, 1998, **120**, 2391–2407.

14 W. Adam, H. Garcia, V. Marti and J. N. Moorthy, *J. Am. Chem. Soc.*, 1999, **121**, 9475–9476.

15 M. B. Reyes and B. K. Carpenter, *J. Am. Chem. Soc.*, 2000, **122**, 10163–10176.

16 A. Sinicropi, C. S. Page, W. Adam and M. Olivucci, *J. Am. Chem. Soc.*, 2003, **125**, 10947–10959.

17 W. Adam, M. Diedering and A. V. Trofimov, *J. Phys. Org. Chem.*, 2004, **17**, 643–655.

18 M. Abe, C. Ishihara, S. Kawanami and A. Masuyama, *J. Am. Chem. Soc.*, 2005, **127**, 10–11.

19 S. Yagi, Y. Hiraga, R. Takagi and M. Abe, *J. Phys. Org. Chem.*, 2011, **24**, 894–901.

20 K. S. Khuong and K. N. Houk, *J. Am. Chem. Soc.*, 2003, **125**, 14867–14883.

21 M. Hamaguchi, M. Nakaishi, T. Nagai, T. Nakamura and M. Abe, *J. Am. Chem. Soc.*, 2007, **129**, 12981–12988.

22 C. Ishihara and M. Abe, *Aust. J. Chem.*, 2010, **63**, 1615–1618.

23 P. L. A. Popelier and E. A. G. Bremond, *Int. J. Quantum Chem.*, 2009, **109**, 2542–2553.

24 R. F. W. Bader, *Atoms in molecules: a quantum theory*, Clarendon Press, Oxford, New York, 1990.

25 R. F. W. Bader, T. T. Nguyendang and Y. Tal, *Rep. Prog. Phys.*, 1981, **44**, 893–948.

26 X. Krokidis, S. Noury and B. Silvi, *J. Phys. Chem. A*, 1997, **101**, 7277–7282.

27 A. D. Becke and K. E. Edgecombe, *J. Chem. Phys.*, 1990, **92**, 5397–5403.

28 B. Silvi and A. Savin, *Nature*, 1994, **371**, 683–686.

29 R. Thom, *Structural stability and morphogenesis, an outline of a general theory of models*, W. A. Benjamin, 1st edn, 1975 Reading, Mass.

30 V. Polo, P. Gonzalez-Navarrete, B. Silvi and J. Andres, *Theor. Chem. Acc.*, 2008, **120**, 341–349.

31 J. Andres, S. Berski, L. R. Domingo and P. Gonzalez-Navarrete, *J. Comput. Chem.*, 2012, **33**, 748–756.

32 P. Gonzalez-Navarrete, L. R. Domingo, J. Andres, S. Berski and B. Silvi, *J. Comput. Chem.*, 2012, **33**, 2400–2411.

33 P. Gonzalez-Navarrete, F. R. Sensato, J. Andres and E. Longo, *J. Phys. Chem. A*, 2014, **118**, 6092–6103.

34 J. Andres, S. Berski, L. R. Domingo, V. Polo and B. Silvi, *Curr. Org. Chem.*, 2011, **15**, 3566–3575.

35 S. Berski, F. R. Sensato, V. Polo, J. Andres and V. S. Safont, *J. Phys. Chem. A*, 2011, **115**, 514–522.

36 V. Polo, J. Andres, S. Berskit, L. R. Domingo and B. Silvi, *J. Phys. Chem. A*, 2008, **112**, 7128–7136.

37 V. Polo and J. Andres, *J. Comput. Chem.*, 2005, **26**, 1427–1437.

38 V. Polo, J. Andres, R. Castillo, S. Berski and B. Silvi, *Chem. – Eur. J.*, 2004, **10**, 5165–5172.

39 V. Polo, J. Andres and B. Silvi, *J. Comput. Chem.*, 2007, **28**, 857–864.

40 V. Polo, L. R. Domingo and J. Andres, *J. Phys. Chem. A*, 2005, **109**, 10438–10444.

41 V. Polo, L. R. Domingo and J. Andres, *J. Org. Chem.*, 2006, **71**, 754–762.

42 J. C. Santos, J. Andres, A. Aizman, P. Fuentealba and V. Polo, *J. Phys. Chem. A*, 2005, **109**, 3687–3693.

43 P. González-Navarrete, J. Andrés and S. Berski, *J. Phys. Chem. Lett.*, 2012, **3**, 2500–2505.

44 M. J. Frisch, H. B. Schlegel, G. E. Scuseria, J. R. C. M. A. Robb, G. Scalmani, V. Barone, B. Mennucci, H. N. G. A. Petersson, M. Caricato, X. Li, H. P. Hratchian, J. B. A. F. Izmaylov, G. Zheng, J. L. Sonnenberg, M. Hada, K. T. M. Ehara, R. Fukuda, J. Hasegawa, M. Ishida, T. Nakajima, O. K. Y. Honda, H. Nakai, T. Vreven, J. A. Montgomery, Jr., F. O. J. E. Peralta, M. Bearpark, J. J. Heyd, E. Brothers, V. N. S. K. N. Kudin, T. Keith, R. Kobayashi, J. Normand, A. R. K. Raghavachari, J. C. Burant, S. S. Iyengar, J. Tomasi, N. R. M. Cossi, J. M. Millam, M. Klene, J. E. Knox, J. B. Cross, C. A. V. Bakken, J. Jaramillo, R. Gomperts, R. E. Stratmann, A. J. A. O. Yazyev, R. Cammi, C. Pomelli, J. W. Ochterski, K. M. R. L. Martin, V. G. Zakrzewski, G. A. Voth, J. J. D. P. Salvador, S. Dapprich, A. D. Daniels, J. B. F. O. Farkas, J. V. Ortiz, and J. Cioslowski, D. J. Fox, Gaussian 09, Inc., Wallingford, CT, 2010.

45 A. D. Becke, *Phys. Rev. A: At., Mol., Opt. Phys.*, 1988, **38**, 3098–3100.

46 A. D. Becke, *J. Chem. Phys.*, 1993, **98**, 5648.

47 C. T. Lee, W. T. Yang and R. G. Parr, *Phys. Rev. B: Condens. Matter Mater. Phys.*, 1988, **37**, 785–789.

48 Y. Zhao, N. E. Schultz and D. G. Truhlar, *J. Chem. Theory Comput.*, 2006, **2**, 364–382.

49 K. Fukui, *J. Phys. Chem.*, 1970, **74**, 4161–4163.

50 K. Fukui, *Acc. Chem. Res.*, 1981, **14**, 363–368.

51 S. Noury, X. Krokidis, F. Fuster and B. Silvi, *Comput. Chem.*, 1999, **23**, 597–604.

52 E. F. Pettersen, T. D. Goddard, C. C. Huang, G. S. Couch, D. M. Greenblatt, E. C. Meng and T. E. Ferrin, *J. Comput. Chem.*, 2004, **25**, 1605–1612.

53 R. Bauernschmitt and R. Ahlrichs, *J. Chem. Phys.*, 1996, **104**, 9047–9052.

54 R. Caballol, O. Castell, F. Illas, P. R. Moreira and J. P. Malrieu, *J. Phys. Chem. A*, 1997, **101**, 7860–7866.
55 L. Noodleman, *J. Chem. Phys.*, 1981, **74**, 5737–5743.
56 J. Andres, P. Gonzalez-Navarrete and V. Sixte Safont, *Int. J. Quatum. Chem.*, 2014, **114**, 1239–1252.
57 J. Andrés, L. Gracia, P. González-Navarrete and V. S. Safont, *Comput. Theor. Chem.*, 2015, **1053**, 17–30.
58 B. Silvi, *J. Mol. Struct.*, 2002, **614**, 3–10.
59 S. Berski, J. Andres, B. Silvi and L. R. Domingo, *J. Phys. Chem. A*, 2006, **110**, 13939–13947.
60 J. Melin and P. Fuentealba, *Int. J. Quatum. Chem.*, 2003, **92**, 381–390.
61 I. Viciano, P. González-Navarrete, J. Andrés and S. Martí, *J. Chem. Theory Comput.*, 2015, **11**, 1470–1480.